

ON THE CONVERGENCE OF ITERATIVE REGULARIZATION METHOD ASSISTED BY THE GRAPH LAPLACIAN WITH EARLY STOPPING *

HARSHIT BAJPAI[†], GAURAV MITTAL[‡], AND ANKIK KUMAR GIRI[†]

Abstract. We present a data-assisted iterative regularization method for solving ill-posed inverse problems in Hilbert space settings. The proposed approach, termed **IRMGL+ Ψ** , integrates classical iterative techniques with a data-driven regularization term realized through an iteratively updated graph Laplacian. Our method commences by computing a preliminary solution using any suitable reconstruction method, which then serves as the basis for constructing the initial graph Laplacian. The solution is subsequently refined through an iterative process, where the graph Laplacian is simultaneously recalibrated at each step to effectively capture the evolving structure of the solution. A key innovation of this work lies in the formulation of this iterative scheme and the rigorous justification of the classical discrepancy principle as a reliable early stopping criterion specifically tailored to the proposed method. Under standard assumptions, we establish stability and convergence results for the scheme when the discrepancy principle is applied. Furthermore, we demonstrate the robustness and effectiveness of our method through numerical experiments utilizing four distinct initial reconstructors Ψ : the adjoint operator (Adj), filtered back projection (FBP), total variation (TV) denoising, and standard Tikhonov regularization (Tik). It is observed that **IRMGL+Adj** demonstrates a distinct advantage over the other initializers, producing a robust and stable approximate solution directly from a basic initial reconstruction.

Key words. Iterative regularization, Graph Laplacian operator, Data-assisted regularization, Ill-posed problems, Discrepancy principle, Medical imaging

MSC codes. 47A52, 65F22, 05C90, 65J20

1. Introduction. This work is concerned with the analysis and numerical solution of a linear ill-posed inverse problem, modeled by the operator equation

$$(1.1) \quad Au = v,$$

where $A : \mathcal{D}(A) \subset \mathcal{U} \rightarrow \mathcal{V}$ is a bounded linear operator between real Hilbert spaces \mathcal{U} and \mathcal{V} , and $\mathcal{D}(A)$ denotes the domain of A . Unless otherwise specified, we assume that both spaces are equipped with the standard inner product $\langle \cdot, \cdot \rangle$ and corresponding norm $\| \cdot \|$. Given a fixed u^\dagger and the corresponding exact data $v := Au^\dagger$ our goal is to recover a good approximation of u^\dagger from noisy observations v^δ to v (unknown in practical applications) which satisfies

$$(1.2) \quad \|v^\delta - v\| \leq \delta$$

with the known noise level $\delta > 0$. In practical applications, (1.1) is typically ill-posed, meaning that even small perturbations in the data can lead to disproportionately large deviations in the resulting solution. Therefore, regularization techniques are essential to ensure the stability and reliability of the approximate solution. Many of these approaches can be classified as Tikhonov-type variational methods, which are typically formulated as

$$(1.3) \quad u_\alpha^\delta := \arg \min_{u \in \mathcal{U}} \{ \mathfrak{D}(Au; v^\delta) + \alpha \mathfrak{R}(u) \},$$

*Submitted to the editors DATE.

Funding: This work was funded by the ANRF through grant CRG/2022/00549.

[†]Department of Mathematics, Indian Institute of Technology Roorkee, Roorkee, 247667, India (harshit_b@ma.iitr.ac.in, ankik.giri@ma.iitr.ac.in).

[‡]Defence Research and Development Organization, Near Metcalfe House, Delhi, 110054, India (gaurav.mittaltwins@yahoo.com).

where $\mathfrak{D}(\cdot; \cdot)$ denotes a pseudo-distance measuring the discrepancy between the forward model Au and the observed (possibly noisy) data v^δ . The term $\mathfrak{R}(u)$ serves as a regularization functional, and the regularization parameter $\alpha > 0$ governs the trade-off between the influence of the data misfit and regularization. A common choice for these terms is

$$\mathfrak{D}(Au; v^\delta) = \frac{1}{2} \|Au - v^\delta\|_2^2, \quad \mathfrak{R}(u) = \|u\|_1,$$

where the ℓ_2 -norm ensures a least-squares fit to the data, and the ℓ_1 -norm promotes sparsity in the solution. For further details, we refer the reader to [16] and [40].

The choice of the regularization functional \mathfrak{R} plays a pivotal role in the success of the reconstruction. When prior knowledge about the true solution is available, \mathfrak{R} can be specifically designed to incorporate this information, thereby steering the regularization process toward a restricted class of solutions that exhibit the desired features or structures. Few prominent examples of regularization functionals are as follows.

- $\mathfrak{R}(u) = \|u - u^{(0)}\|_2^2$, where $\|\cdot\|_2$ is the Euclidean norm. This choice is particularly effective when the prior information $u^{(0)}$ about the true solution is available. For further details, see [6, 31, 39].
- $\mathfrak{R}(u) = \|Lu\|_q^q$, where $q \geq 1$, $\|\cdot\|_q$ is the Euclidean q -norm and L denotes a linear differential operator. This choice is especially valuable in imaging applications, as differential operators are capable of capturing sharp variations such as edges or intensity discontinuities. See [20, 21, 34] for the references.
- $\mathfrak{R}(u) = \|Mu - v^\delta\|_2^2$, where M is a data-driven operator constructed from a prior dataset $\{(u^{(i)}, Au^{(i)})\}_{1 \leq i \leq l}$, such that $Mu^{(i)} := Au^{(i)}$ for each i . This approach is particularly useful in scenarios where the underlying physical or technical model is not fully understood, as it leverages empirical data to inform the regularization process. See [3, 4, 5, 7] for the references.

Digital images, formed by pixels organized on a two-dimensional grid, naturally lend themselves to a graph-based representation. In light of this, graph-based differential operators Δ have emerged in recent years as effective substitutes for traditional Euclidean differential operators L , particularly in image processing, image denoising and computed tomography (CT) problems, see [11, 9, 10, 12, 14, 17, 18, 30, 36, 44]. Graph-based operators have demonstrated consistently strong performance, largely due to their ability to more accurately capture the complex structures and textures inherent in image data. In contrast to traditional Euclidean differential operators, which rely primarily on spatial proximity, graph-based methods incorporate both spatial and intensity similarities between pixels. This enables a more nuanced representation of image content and facilitates richer information extraction. For a detailed discussion on graph-based operators, the reader is referred to Section 2.

A critical aspect in graph-based regularization methods is the construction of the graph from a signal that effectively captures the key features of the ground truth u^\dagger . As highlighted in [30], directly constructing the graph S from the observed, noisy data v^δ often leads to suboptimal performance in imaging tasks such as tomographic reconstruction and deblurring. This shortcoming arises because v^δ resides in a different domain than u^\dagger . To mitigate this issue, the authors proposed a preprocessing step that transforms v^δ into a more suitable representation $\Psi(v^\delta)$, from which the graph is then constructed. The mapping $\Psi : \mathcal{V} \rightarrow \mathcal{U}$ serves as a reconstruction operator that lifts the observations from \mathcal{V} into \mathcal{U} , where the ground truth signal lives. This transformation can be realized using standard techniques such as Tikhonov filtering [16] or the filtered backprojection (FBP) method [28], depending on the specific

inverse problem. In a similar vein, and independently, iterative schemes that adaptively update the graph weights during the reconstruction process were proposed in [2, 11, 35, 36, 44].

Despite providing a coherent and principled optimization framework for solving inverse problem (1.1), variational regularization methods of the form (1.3) have a significant number of drawbacks in comparison to iterative methods. The selection of an appropriate regularization parameter α remains a critical and often challenging task in variational methods, with poor choices leading to suboptimal reconstructions. Furthermore, these methods tend to be computationally intensive, particularly in high-dimensional settings. In contrast, iterative regularization methods inherently offer greater flexibility through adaptive regularization via early stopping rules. They are typically easier to implement, more scalable, and naturally suited for incorporating data-driven components.

To effectively address these challenges, we propose a novel iterative scheme, referred to as the *Iterative Regularization Method assisted by the Graph Laplacian* (**IRMGL+ Ψ** , see also Fig. 1), which performs the following iterative updates

$$(1.4) \quad \begin{cases} u_{k+1}^\delta = u_k^\delta - \alpha_k^\delta A^*(Au_k^\delta - v^\delta) - \beta_k^\delta \Delta_{u_k^\delta} u_k^\delta, & k \in \mathbb{N}, \\ u_0^\delta = \Psi(v^\delta), \end{cases}$$

where $\Psi : \mathcal{V} \rightarrow \mathcal{U}$ is the initial reconstructor, A^* denotes the adjoint of A , Δ_u is a graph Laplacian build from u (see Subsection 2.2 for a proper definition) and $\alpha_k^\delta > 0$, $\beta_k^\delta \geq 0$ are suitably chosen step sizes and weighted parameters, respectively. The detailed discussion on the method can be found in Subsection 3.1. Note that, this method is obtained from a gradient descent applied on a functional

$$J(u) := \frac{1}{2} \|Au - v^\delta\|^2 + \beta \langle u, \Delta_u u \rangle.$$

where $\beta \geq 0$ is a constant. It is crucial to highlight that the proposed scheme (1.4) serves as the iterative counterpart to the existing **graphLa+ Ψ** [12] and **it-graphLa Ψ** [11] frameworks.

Both **graphLa+ Ψ** (which is based on a variational framework) and **it-graphLa Ψ** (developed for acoustic impedance inversion by incorporating an iterated graph Laplacian into a variational regularization framework) require solving a minimization problem at each step. While [11] provided numerical evidence for their approach, a rigorous mathematical justification was not established. In contrast, our proposed **IRMGL+ Ψ** method presents a distinct advancement: it offers an inherently iterative and robust solution by circumventing the need to solve computationally intensive minimization problems, a characteristic of the aforementioned works [11, 12]. Crucially, this work also addresses a critical theoretical void by furnishing comprehensive convergence and stability proofs for our scheme. The details on the implementation of these two methods are provided in the Subsection 4.3 to enable a comparative visualization with our scheme. Moreover, **IRMGL+ Ψ** can also be interpreted as a generalization of the classical Landweber method [19], where the extension arises from the incorporation of a data-driven term induced by the graph Laplacian.

Due to the ill-posedness of (1.1), the iterative process must not be carried out indefinitely. Instead, it requires a suitable termination strategy, a concept widely known as *early stopping* in the field of inverse problems and machine learning [16]. It is now widely recognized that early stopping is a critical aspect that must be carefully addressed in the design of image reconstruction models [8, 23, 43].

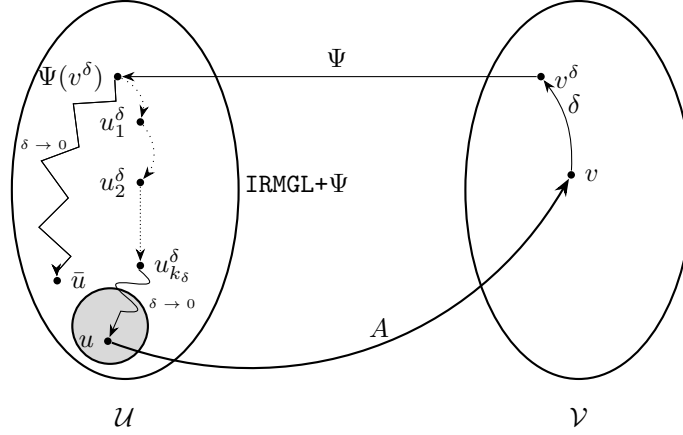


Fig. 1: An abstract illustration of the $\text{IRMGL}+\Psi$ method. The initial reconstructor Ψ does not necessarily serve as a regularization method, as indicated by the piecewise linear trajectory of $\Psi(v^\delta)$ as $\delta \rightarrow 0$. However, when combined with $\text{IRMGL}+\Psi$, the resulting process constitutes a stable and convergent regularization method. The dotted trajectory represents the iterative progression of the method, while the approximate solution at iteration k_δ is denoted by $u_{k_\delta}^\delta$. The coiled path illustrates the regularization behavior of the method, highlighting the convergence $u_{k_\delta}^\delta \rightarrow u$ as $\delta \rightarrow 0$. Full mathematical justification for the convergence is given in subsequent sections. The difference between $\text{IRMGL}+\Psi$ and $\text{GraphLa}+\Psi$ can be noted using [12, Fig. 1.1].

To serve the purpose, we employ the discrepancy principle [32], which suggests that the iteration should be terminated once the residual norm becomes comparable to the noise level δ . Hence the stopping index $k_\delta = k(\delta, v^\delta)$ determined by the discrepancy principle is defined as

$$(1.5) \quad k_\delta := \min \{k \geq 0 : \|Au_k^\delta - v^\delta\| \leq \tau\delta\},$$

where $\tau > 1$ is a known constant. This principle is applicable whenever concrete value of δ (noise level) is available, which can often be inferred directly from the data. The above equation outputs k_δ , so we use $u_{k_\delta}^\delta$ as an approximate solution of (1.1). We investigate the convergence behavior of the $\text{IRMGL}+\Psi$ method under the discrepancy principle (1.5) and we establish that the discrepancy principle guarantees termination of the iteration after a finite number of steps. Furthermore, we introduce a systematic criterion for choosing the parameters α_k^δ and β_k^δ . The proposed parameter selection strategy is adaptive in nature, utilizing only information that is intrinsically available during the iterative process.

It is worth noting that the data-driven term in $\text{IRMGL}+\Psi$ method (1.4) inherently depends on both the noise level δ and the observed data v^δ . This dual dependence introduces additional complexity into the analysis, rendering it highly nonstandard from existing iterative regularization methods [27].

The paper is structured as follows. Section 2 introduces the necessary notation and provides preliminaries related to graphs and image representations. In Section 3, we describe the proposed method in detail, including an algorithmic formulation, and formulate the conditions under which convergence is ensured. We also prove the

stability and convergence of the method within this section. Section 4 is dedicated to demonstrating the effectiveness of the proposed approach through a series of numerical experiments, highlighting its advantages over variational-type methods assisted by graph Laplacian regularization. Finally, we summarize our contributions and discuss potential directions for future research in Section 5.

2. Preliminaries. In this section, we present foundational definitions and results that are related to this work. We begin in subsection 2.1 by outlining essential concepts from graph theory. One may refer to [29] for more details.

2.1. Graph theory.

DEFINITION 2.1. *For a finite set S , we define a graph over S as a pair $G = (S, w)$, where $w : S \times S \rightarrow [0, \infty)$ is called edge-weight function if for every $a, b \in S$, it satisfies*

- *Symmetry:* $w(a, b) = w(b, a)$,
- *No self-loops:* $w(a, a) = 0$.

The set of edges is given by $T := \{(a, b) \in S \times S \mid w(a, b) \neq 0\}$. Two nodes a and b are said to be connected if $w(a, b) > 0$. In such cases, we denote this relation by $a \sim b$. This weight $w(a, b)$ measures how strongly nodes a and b are connected.

DEFINITION 2.2 (Graph Laplacian). *For any function $\mathbf{x} : S \rightarrow \mathbb{R}$, the graph Laplacian $\Delta \mathbf{x} : S \rightarrow \mathbb{R}$ associated to the graph $G = (S, w)$ is defined by the action*

$$(2.1) \quad \Delta \mathbf{x}(a) := \sum_{a \sim b} w(a, b)(\mathbf{x}(a) - \mathbf{x}(b)).$$

The corresponding graph Laplacian matrix for the operator Δ is given by

$$(2.2) \quad \Delta := D - W,$$

where $W = [w(a_i, a_j)]_{\{i, j \in |S|\}}$ is the *weight matrix* and D is the *diagonal degree matrix* with diagonal entries $d_{ii}(a_i) = \sum_{j \in |S|} w(a_i, a_j)$. Here $|S|$ denotes the cardinality of the set S . It can be noted that Δ defined in (2.2) applied on $\mathbf{x}(a)$ will give the same action as in (2.1).

2.2. Images and graphs. This subsection goes over the fundamental ideas needed to create a graph from an image. Notably, defining a graph necessitate an edge-weight function w and a set of nodes S .

The union of multiple pixels $a \in S$ arranged on a grid creates an image, so it makes sense to identify pixels as an ordered pair $a = (i_a, j_a)$ with $i_a = 1, \dots, p$ and $j_a = 1, \dots, q$. In this case, p and q represent the total number of pixels along the horizontal and vertical axes, respectively. Thus, the node can be configured as

$$S = \{a \mid a = (i_a, j_a), i_a = 1, \dots, p, j_a = 1, \dots, q\}.$$

For simplicity, we consider a grayscale image, which is characterized by the intensity values of its pixels. Such an image can be represented as a function that assigns an intensity value to each pixel location, i.e.,

$$\mathbf{x} : S \rightarrow [0, 1],$$

where 0 corresponds to black, 1 corresponds to white, and intermediate values represent varying shades of gray. A widely used method for connecting two pixels by w

based on their spatial proximity and light intensity is provided by

$$(2.3) \quad w_{\mathbf{x}}(a, b) = \underbrace{g(a, b)}_{\text{geometry}} \times \underbrace{h_{\mathbf{x}}(a, b)}_{\mathbf{x}\text{-intensity}},$$

where $g(a, b)$ denotes an edge weight function determined by the geometric characteristic of S . A commonly used form of g is

$$g(a, b) = \mathbf{1}_{(0, R]}(\tilde{\mathcal{O}}(a, b))$$

where $\mathbf{1}_{(0, R]}$ denotes the indicator function, $R > 0$ is a control parameter specifying the maximum allowable distance for two pixels to be considered neighbors, and $\tilde{\mathcal{O}}(a, b)$ represents the distance between pixels a and b . The common choices are $\tilde{\mathcal{O}}(a, b) = |i_a - i_b| + |j_a - j_b|$ or $\tilde{\mathcal{O}}(a, b) = \max\{|i_a - i_b|, |j_a - j_b|\}$. The function $h_{\mathbf{x}}(a, b)$ serves to weight the connection between two pixels based on their intensity values and for that, in general, Gaussian kernel function is used. That is

$$h_{\mathbf{x}}(a, b) := \exp\left(\frac{-|\mathbf{x}(a) - \mathbf{x}(b)|^2}{\sigma}\right),$$

where $\sigma > 0$ is the control parameter. We refer to [13, 15, 18, 30] for a thorough description of how to define the weights of the graph Laplacian using such a Gaussian kernel function. A similar construction of a graph induced by a grayscale image is given in [11, 12]. In Example 2.3, we present the process of constructing a graph and the corresponding graph Laplacian for a 2×2 grayscale image (see also Fig. 2).

Example 2.3. Consider a 2×2 grayscale image with pixel intensities given as in Table 1. This image corresponds a function $\mathbf{x} : S \rightarrow [0, 1]$, where each pixel

$i \backslash j$	0	1
0	0.2	0.3
1	0.5	0.1

Table 1: Pixel values indexed by (i, j)

$a = (i, j) \in S$ has an intensity value $\mathbf{x}(a)$. Here $S = \{a_1 = (0, 0), a_2 = (0, 1), a_3 = (1, 0), a_4 = (1, 1)\}$ and we will use (2.3) to define the edge weight function with $\tilde{\mathcal{O}}(a, b) = |i_a - i_b| + |j_a - j_b|$, $R = 1$ (so only immediate neighbors are connected) and $\sigma = 0.01$ (for visible weight variation). Under these conditions, the weight matrix W and diagonal degree matrix D are given as

$$W = \begin{bmatrix} 0 & 0.3679 & 0.0001 & 0 \\ 0.3679 & 0 & 0 & 0.0183 \\ 0.0001 & 0 & 0 & 0.0000 \\ 0 & 0.0183 & 0.0000 & 0 \end{bmatrix}, D = \begin{bmatrix} 0.3680 & 0 & 0 & 0 \\ 0 & 0.3861 & 0 & 0 \\ 0 & 0 & 0.0001 & 0 \\ 0 & 0 & 0 & 0.0183 \end{bmatrix}.$$

Further, using (2.2), we can calculate the graph Laplacian $\Delta_{\mathbf{x}}$ of \mathbf{x} .

We also refer to Fig. 3 and Fig. 4 for a true image in grayscale and its step-by-step conversion to its graph representation, respectively. Moreover, Fig. 5 shows the true grayscale image and magnitude of its graph Laplacian.

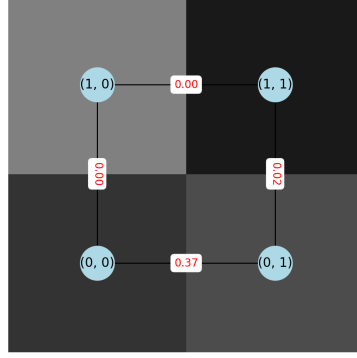


Fig. 2: 2×2 grayscale image with an induced graph. Each node corresponds to a pixel and the red edge labels indicate the weights based on similarity and spatial proximity.



Fig. 3: True image in grayscale.

3. The iterative regularization method assisted by graph Laplacian. In this section, we propose and analyze a novel iterative regularization method that incorporates graph Laplacian-based information, referred to as **IRMGL+ Ψ** . We conduct a rigorous convergence analysis of the method and examine its regularization properties when combined with a standard a posteriori stopping criterion (1.5). The following baseline assumptions on the forward operator A are imposed.

Assumption 3.1. $A : \mathcal{D}(A) \subset \mathcal{U} \rightarrow \mathcal{V}$ is a bounded linear operator.

Assumption 3.2. There exists $u^\dagger \in \mathcal{B}(u_0, \varphi)$ such that $Au^\dagger = v$, where $\mathcal{B}(u_0, \varphi) := \{u \in \mathcal{U} : \|u - u_0\| \leq \varphi\}$ denotes a closed ball of radius φ centered at u_0 .

3.1. The method. In this subsection, we present a detailed description of the proposed **IRMGL+ Ψ** method (1.4).

Let us begin by introducing the step size α_k^δ and the weighted parameter β_k^δ to promote rapid convergence of the method (1.4). It is natural to select α_k^δ and β_k^δ adaptively at each iteration in such a way that the iterates remain close to a solution of (1.1).

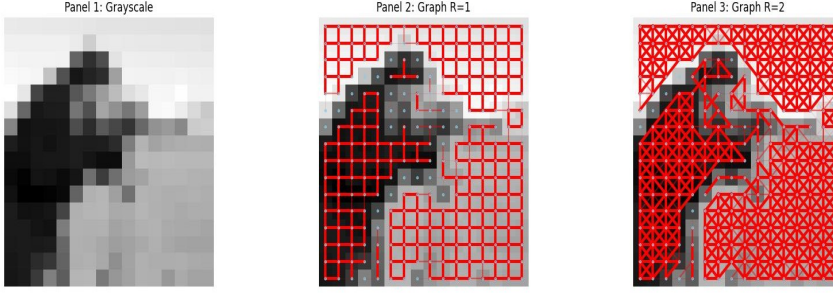


Fig. 4: This figure provides a step-by-step illustration of the process of converting an image \mathbf{x} into a graph representation. On left, a 16×16 grayscale image is displayed, where the intensity of each pixel is determined by the function \mathbf{x} , which encapsulates the underlying image information. In second panel, each pixel is mapped to a graph node (depicted as a sky blue circle), with its location corresponding to its discrete position in the grid \mathbb{Z}^2 . Edges between nodes are then constructed using the data-dependent weight function $w_{\mathbf{x}}(a, b)$, parameterized by $R = 1$ and $\sigma = 0.005$, which quantifies similarity based on pixel intensities. The strength of these connections is visually represented by the thickness of red edges: thicker edges indicate higher similarity between adjacent pixels, while thinner edges reflect greater dissimilarity. The right panel illustrates the effect of increasing the neighborhood radius to $R = 2$, resulting in a denser connectivity pattern that incorporates a broader local context.

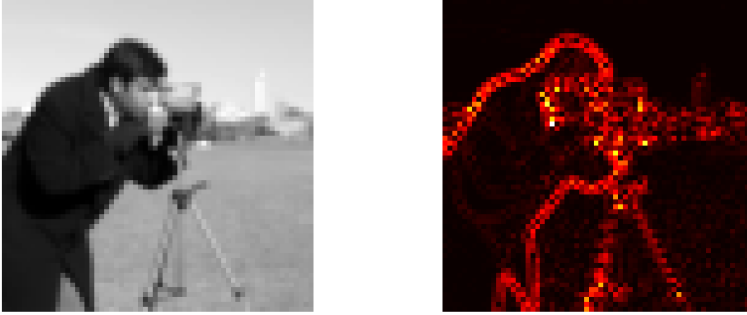


Fig. 5: The left panel shows a 64×64 grayscale image. The right panel displays the magnitude of the graph Laplacian, $|\Delta_{\mathbf{x}} \mathbf{x}|$, computed using (2.1). This visualization effectively highlights the edge information. The ‘hot’ colormap is used, which maps low values to black and progressively higher values through red, orange, yellow, and white, emphasizing areas with significant local intensity variation.

Accordingly, we define the parameters

$$(3.1) \quad 0 < \eta \leq \alpha_k^\delta = \begin{cases} \min \left\{ \frac{\eta_0 \|Au_k^\delta - v^\delta\|^2}{\|A^*(Au_k^\delta - v^\delta)\|^2}, \eta_1 \right\}, & \text{if } \|A^*(Au_k^\delta - v^\delta)\| \neq 0 \\ 0, & \text{if } \|A^*(Au_k^\delta - v^\delta)\| = 0 \end{cases}$$

$$(3.2) \quad \beta_k^\delta = \begin{cases} \min \left\{ \frac{\nu_0 \|Au_k^\delta - v^\delta\|^2}{\|\Delta_{u_k^\delta} u_k^\delta\|}, \frac{\nu_1}{\|\Delta_{u_k^\delta} u_k^\delta\|}, \nu_2 \right\}, & \text{if } \|\Delta_{u_k^\delta} u_k^\delta\| \neq 0 \\ 0, & \text{if } \|\Delta_{u_k^\delta} u_k^\delta\| = 0, \end{cases}$$

where $\eta_0, \eta_1, \nu_0, \nu_1$ and ν_2 are some fixed positive constants. The pseudo code of the iterative scheme (1.4) is outlined in Algorithm 3.1.

Remark 3.3. At each $(k+1)$ -th iteration of the Algorithm 3.1, a new graph Laplacian $\Delta_{u_k^\delta}$ is constructed based on the previous approximate solution u_k^δ , for any given initial reconstructor Ψ . In other words, the regularization term is adaptively updated at each iteration.

Algorithm 3.1 IRMGL+ Ψ with early stopping

Given: $A, v^\delta, \delta, \Psi, \sigma, R$.
Initialize: $u_0^\delta = \Psi(v^\delta)$
while $\|Au_k^\delta - v^\delta\| > \tau\delta$ **do**
 Given u_k^δ, R, σ , compute $\Delta_{u_k^\delta}$ as defined in Section 2.
 Update $u_{k+1}^\delta = u_k^\delta - \alpha_k^\delta A^*(Au_k^\delta - v^\delta) - \beta_k^\delta \Delta_{u_k^\delta} u_k^\delta$,
 where α_k^δ and β_k^δ are defined in (3.1) and (3.2), respectively.
end while
return $u_{k_\delta}^\delta$.

LEMMA 3.4. *Let Assumption 3.1 and 3.2 hold. Consider Algorithm 3.1 and let $n \leq k_\delta$ be an integer, where k_δ is the stopping index as defined in (1.5). Let*

$$(3.3) \quad C := \eta - \frac{\eta_1}{\tau} - \nu_0(\wp + \nu_1) - \eta_0\eta_1 > 0.$$

Then the following hold:

(i) *The monotone behavior of the iterates of IRMGL+ Ψ (1.4) for $0 \leq k < n$, i.e.,*

$$\|u_{k+1}^\delta - u^\dagger\| \leq \|u_k^\delta - u^\dagger\|.$$

(ii) *The iterates $u_k^\delta \in \mathcal{B}(u^\dagger, \wp)$ for all $0 \leq k \leq n$ and*

$$\sum_{k=0}^n \|Au_k^\delta - v^\delta\|^2 \leq \frac{1}{2C} \|u_0^\delta - u^\dagger\|^2.$$

Proof. By Assumption 3.2, we have $u_0 \in \mathcal{B}(u^\dagger, \wp)$. Suppose further that $u_k^\delta \in \mathcal{B}(u^\dagger, \wp)$ for some iteration k . This implies that $u_k^\delta \in \mathcal{B}(u_0, 2\wp)$. We define

$$x_k^\delta := u_k^\delta - u^\dagger \quad \text{and} \quad d_k^\delta := \alpha_k^\delta A^*(Au_k^\delta - v^\delta) + \beta_k^\delta \Delta_{u_k^\delta} u_k^\delta.$$

With these definitions and in view of the update rule given in (1.4), we obtain

$$(3.4) \quad \|x_{k+1}^\delta\|^2 - \|x_k^\delta\|^2 = \|d_k^\delta\|^2 - 2\langle x_k^\delta, d_k^\delta \rangle.$$

We now proceed to analyze each term on the right-hand side of the (3.4) individually.

To begin, we consider the second term and estimate it as

$$\begin{aligned}
-\langle x_k^\delta, d_k^\delta \rangle &= \alpha_k^\delta \langle A(u^\dagger - u_k^\delta), Au_k^\delta - v^\delta \rangle + \beta_k^\delta \langle u^\dagger - u_k^\delta, \Delta_{u_k^\delta} u_k^\delta \rangle \\
&= -\alpha_k^\delta \|Au_k^\delta - v^\delta\|^2 + \alpha_k^\delta \langle v - v^\delta, Au_k^\delta - v^\delta \rangle + \beta_k^\delta \langle u^\dagger - u_k^\delta, \Delta_{u_k^\delta} u_k^\delta \rangle \\
&\leq -\alpha_k^\delta \|Au_k^\delta - v^\delta\|^2 + \alpha_k^\delta \delta \|Au_k^\delta - v^\delta\| + \beta_k^\delta \wp \|\Delta_{u_k^\delta} u_k^\delta\| \\
(3.5) \quad &\leq -\left(\eta - \frac{\eta_1}{\tau}\right) \|Au_k^\delta - v^\delta\|^2 + \wp \nu_0 \|Au_k^\delta - v^\delta\|^2,
\end{aligned}$$

where we have used (1.2), (1.5) and (3.1) in deriving (3.5). Similarly, by using the definitions of α_k^δ and β_k^δ with the inequality $(a_1 + a_2)^2 \leq 2(a_1^2 + a_2^2)$ for $a_1, a_2 \in \mathbb{R}$, we can estimate the first term of (3.4) as

$$\begin{aligned}
\|d_k^\delta\|^2 &= \|\alpha_k^\delta A^*(Au_k^\delta - v^\delta) + \beta_k^\delta \Delta_{u_k^\delta} u_k^\delta\|^2 \\
&\leq 2\eta_0 \eta_1 \|Au_k^\delta - v^\delta\|^2 + 2\nu_0 \nu_1 \|Au_k^\delta - v^\delta\|^2 \\
(3.6) \quad &\leq 2(\eta_0 \eta_1 + \nu_0 \nu_1) \|Au_k^\delta - v^\delta\|^2.
\end{aligned}$$

Further, by using (3.5) and (3.6) in (3.4), we get

$$(3.7) \quad \|x_{k+1}^\delta\|^2 - \|x_k^\delta\|^2 \leq -2\left(\eta - \frac{\eta_1}{\tau} - \nu_0(\wp + \nu_1) - \eta_0 \eta_1\right) \|Au_k^\delta - v^\delta\|^2.$$

Finally, by substituting (3.3) in (3.7), we obtain the required monotonicity for $0 \leq k < n$. Next, we discuss the proof of assertion (ii). The inequality (3.7) guarantees that

$$\|u_{k+1}^\delta - u^\dagger\| \leq \|u_k^\delta - u^\dagger\| \leq \wp,$$

which implies that $u_{k+1}^\delta \in \mathcal{B}(u^\dagger, \wp)$. By summing the inequality (3.7) from $k = 0$ to $k = n$, we obtain

$$(3.8) \quad \sum_{k=0}^n [\|x_{k+1}^\delta\|^2 - \|x_k^\delta\|^2] \leq -2C \sum_{k=0}^n \|Au_k^\delta - v^\delta\|^2.$$

Finally, it follows from the last inequality that

$$\sum_{k=0}^n \|Au_k^\delta - v^\delta\|^2 \leq \frac{1}{2C} \|x_0^\delta\|^2 = \frac{1}{2C} \|u_0^\delta - u^\dagger\|^2.$$

This establishes the desired result. \square

In the following result, we show that $\text{IRMGL}+\Psi$ method terminates in a finite number of steps, i.e., Algorithm 3.1 is well defined. The proof leverages Lemma 3.4 to substantiate this conclusion.

THEOREM 3.5. *Let all the assumptions of Lemma 3.4 be satisfied. Let Algorithm 3.1 be initiated with given u_0^δ . Then the algorithm must terminate in finitely many steps, i.e., there exist a finite integer k_δ such that*

$$\|Au_{k_\delta}^\delta - v^\delta\| \leq \tau \delta < \|Au_k^\delta - v^\delta\|, \quad 0 \leq k < k_\delta.$$

Proof. Suppose $n \geq 0$ is an integer such that $\|Au_k^\delta - v^\delta\| > \tau\delta$ holds for all $k = 0, 1, \dots, n$. Then, be engaging (3.8), we obtain

$$\begin{aligned} 2C \sum_{k=0}^{k=n} \|Au_k^\delta - v^\delta\|^2 &\leq \sum_{k=0}^{k=n} [\|x_k^\delta\|^2 - \|x_{k+1}^\delta\|^2], \\ &= \|x_0^\delta\|^2 - \|x_{n+1}^\delta\|^2 \leq \|x_0^\delta\|^2. \end{aligned}$$

By virtue of (1.5), we deduce that

$$(3.9) \quad 2(n+1)C\tau^2\delta^2 \leq 2C \sum_{k=0}^{k=n} \|Au_k^\delta - v^\delta\|^2 \leq \|x_0^\delta\|^2 < \infty.$$

If there exists no finite integer k_δ such that condition (1.5) is satisfied, then by taking the limit as $n \rightarrow \infty$ in (3.9), we get a contradiction. Therefore, Algorithm 3.1 is guaranteed to terminate after a finite number of iterations. \square

3.2. Convergence for exact data. In this subsection, we investigate the counterpart of Algorithm 3.1 in the form of Algorithm 3.2 that employs the exact data v instead of v^δ . To establish the convergence of our method for exact data, we

Algorithm 3.2 IRMGL+ Ψ with exact data

Given: A, v, Ψ, σ, R .

Initialize: $u_0 = \Psi(v)$

while $k \geq 0$ **do**

 Given u_k, R, σ , compute Δ_{u_k} as defined in Section 2.

 Update $u_{k+1} = u_k - \alpha_k A^*(Au_k - v) - \beta_k \Delta_{u_k} u_k$,

 where α_k and β_k are defined as

$$\begin{aligned} \alpha_k &= \min \left\{ \frac{\eta_0 \|Au_k - v\|^2}{\|A^*(Au_k - v)\|^2}, \eta_1 \right\} \quad \text{when } Au_k \neq v, \\ \beta_k &= \begin{cases} \min \left\{ \frac{\nu_0 \|Au_k - v\|^2}{\|\Delta_{u_k} u_k\|}, \frac{\nu_1}{\|\Delta_{u_k} u_k\|}, \nu_2 \right\}, & \text{if } \|\Delta_{u_k} u_k\| \neq 0 \\ 0, & \text{if } \|\Delta_{u_k} u_k\| = 0 \end{cases} \end{aligned}$$

end while

demonstrate that the sequence $\{u_k\}_{k \geq 0}$ generated by Algorithm 3.2 forms a Cauchy sequence. We begin by presenting a preliminary result for the sequence $\{u_k\}_{k \geq 0}$.

LEMMA 3.6. *Let Assumption 3.1 and Assumption 3.2 hold. Let $\{u_k\}_{k \geq 0}$ be the sequence of iterates generated by the Algorithm 3.2. Then $u_k \in \mathcal{B}(u^\dagger, \wp)$ for all integers $k \geq 0$ and for the solution u^\dagger of (1.1), there holds*

$$(3.10) \quad \|u_{k+1} - u^\dagger\|^2 - \|u_k - u^\dagger\|^2 \leq -2C_0 \|Au_k - v\|^2 \quad \forall k \geq 0,$$

where

$$C_0 := \eta - \nu_0(\wp + \nu_1) - \eta_0\eta_1 > 0.$$

Also, the sequence $\{\|u_k - u^\dagger\|\}_{k \geq 0}$ is monotonically decreasing and

$$(3.11) \quad \sum_{k=0}^{\infty} \|Au_k - v\|^2 \leq \frac{1}{2C_0} \|u_0 - u^\dagger\|^2 < \infty.$$

This means that $\|Au_k - v\| \rightarrow 0$ as $k \rightarrow \infty$ i.e., the residual norm converges to zero.

Proof. The result follows directly by analogy with the proof of Lemma 3.4. \square

To this end, we are ready to present the convergence result in the case of $\delta = 0$.

THEOREM 3.7. *Under the assumptions of Lemma 3.6, the iterates $\{u_k\}_{k \geq 0}$ generated by Algorithm 3.2 converges to u^\dagger , which is a solution of (1.1).*

Proof. For $\delta = 0$, we define $x_k := u_k - u^\dagger$ and $r_k := Au_k - v$. Given $l \geq k$, we choose an integer m with $l \geq m \geq k$ such that

$$(3.12) \quad \|r_m\| \leq \|r_n\|, \quad \forall k \leq n \leq l.$$

By triangular inequality, we observe that

$$(3.13) \quad \|x_l - x_k\| \leq \|x_l - x_m\| + \|x_m - x_k\|,$$

where

$$(3.14) \quad \|x_l - x_m\|^2 = 2\langle x_m - x_l, x_m \rangle + \|x_l\|^2 - \|x_m\|^2,$$

$$(3.15) \quad \|x_m - x_k\|^2 = 2\langle x_k - x_m, x_m \rangle + \|x_m\|^2 - \|x_k\|^2.$$

From Lemma 3.6 it is clear that $\{\|x_k\|\}_{k \geq 0}$ is a monotonically decreasing sequence bounded below by 0. Consequently, we suppose that $\lim_{k \rightarrow \infty} \|x_k\| = \theta \geq 0$. Hence, as a result, we write

$$(3.16) \quad \lim_{k \rightarrow \infty} \|x_l - x_m\|^2 = 2 \lim_{k \rightarrow \infty} \langle x_m - x_l, x_m \rangle + \theta^2 - \theta^2,$$

$$(3.17) \quad \lim_{k \rightarrow \infty} \|x_m - x_k\|^2 = 2 \lim_{k \rightarrow \infty} \langle x_k - x_m, x_m \rangle + \theta^2 - \theta^2.$$

Our aim is to demonstrate that $\{x_k\}_{k \geq 0}$ is a Cauchy sequence. To this end, we claim that $\langle x_m - x_l, x_m \rangle \rightarrow 0$ as $k \rightarrow \infty$. For proving the claim, it can be observe that

$$\begin{aligned} |\langle x_m - x_l, x_m \rangle| &= |\langle u_m - u_l, x_m \rangle| \\ &\leq \left| \left\langle \sum_{j=m}^{l-1} \alpha_j A^*(Au_j - v) + \beta_j \Delta_{u_j} u_j, u_m - u^\dagger \right\rangle \right| \\ &\leq \sum_{j=m}^{l-1} |\langle \alpha_j A^*(Au_j - v), u_m - u^\dagger \rangle| + \sum_{j=m}^{l-1} |\langle \beta_j \Delta_{u_j} u_j, u_m - u^\dagger \rangle| \\ &\leq \eta_1 \sum_{j=m}^{l-1} |\langle Au_j - v, Au_m - v \rangle| + \sum_{j=m}^{l-1} \beta_j |\langle \Delta_{u_j} u_j, u_m - u^\dagger \rangle|, \end{aligned}$$

where, we have utilized the bound on α_j and the relation $Au^\dagger = v$ in deriving the last inequality. Furthermore, by incorporating the definition of β_k together with inequality (3.12), and using the fact that $u_k \in \mathcal{B}(u^\dagger, \wp)$ for all $k \geq 0$, the above inequality can be reformulated as

$$\begin{aligned} |\langle x_m - x_l, x_m \rangle| &\leq \eta_1 \sum_{j=m}^{l-1} \|Au_j - v\|^2 + \wp \nu_0 \sum_{j=m}^{l-1} \|Au_j - v\|^2 \\ (3.18) \quad &\leq (\eta_1 + \wp \nu_0) \sum_{j=m}^{l-1} \|Au_j - v\|^2. \end{aligned}$$

Reasoning in the same way for $|\langle x_k - x_m, x_m \rangle|$, we may write

$$(3.19) \quad |\langle x_k - x_m, x_m \rangle| \leq (\eta_1 + \wp \nu_0) \sum_{j=k}^{l-1} \|Au_j - v\|^2.$$

From these estimates, it follows that $|\langle x_m - x_l, x_m \rangle|$ and $|\langle x_k - x_m, x_m \rangle|$ tend to zero as $k \rightarrow \infty$, owing to (3.11). Consequently, from (3.16) and (3.17) it follows that

$$\begin{aligned} \lim_{k \rightarrow \infty} \|x_l - x_m\|^2 &= 2 \lim_{k \rightarrow \infty} \langle x_m - x_l, x_m \rangle = 0, \\ \lim_{k \rightarrow \infty} \|x_m - x_k\|^2 &= 2 \lim_{k \rightarrow \infty} \langle x_k - x_m, x_m \rangle = 0. \end{aligned}$$

Hence, from (3.13), (3.14) and (3.15), it follows that the sequence $\{x_k\}_{k \geq 0}$ is Cauchy. By the definition of x_k , this immediately implies that the sequence $\{u_k\}_{k \geq 0}$ is also Cauchy and therefore converges to some limit \hat{u} . Furthermore, since the residuals $Au_k - v$ tend to zero as $k \rightarrow \infty$, the limit \hat{u} satisfies (1.1), which concludes that $\hat{u} = u^\dagger$. Consequently, the iterates converge to a solution of (1.1). \square

3.3. Stability analysis. In this subsection, we establish the stability of the IRMGL+ Ψ method. For that, we require the following assumption.

Assumption 3.8. Let v^δ be the sequence of noisy data such that $v^\delta \rightarrow v$ as $\delta \rightarrow 0$. Then the reconstructor Ψ satisfies

$$\|\Psi(v^\delta) - \Psi(v)\| \rightarrow 0 \quad \text{as } \delta \rightarrow 0.$$

It is worth noting that the above assumption is relatively mild and is satisfied by a broad class of reconstruction operators. A straightforward example is to consider Ψ as a (locally) Lipschitz continuous operator. That is, if Ψ satisfies

$$\|\Psi(v^\delta) - \Psi(v)\| \leq K \|v^\delta - v\|,$$

for some constant $K > 0$, then the assumption is clearly fulfilled. The following remark presents another example that satisfies Assumption 3.8.

Remark 3.9. A standard Tikhonov regularization method may also serve as a viable choice for the initial reconstructor Ψ . Specifically, one may define

$$(3.20) \quad \Psi(v^\delta) = (A^T A + \gamma I)^{-1} A^T v^\delta,$$

where $\gamma > 0$ is the regularization parameter.

The main difficulty in establishing stability results stems from the regularization term $\mathcal{R}(u, v^\delta)$, which explicitly depends on the observed data v^δ . Consequently, conventional analytical techniques cannot be applied in a straightforward manner and hence we propose a lemma that plays a crucial role in the stability analysis. It is worth noting that a similar result was established in [12] for the variational setting, however, the analysis presented here is fundamentally different from that work.

LEMMA 3.10. *For the iterates u_k^δ and u_k generated by Algorithm 3.1 and Algorithm 3.2 respectively, it holds that*

$$\|\Delta_{u_k^\delta} u_k - \Delta_{u_k} u_k\|_2 \leq \mathcal{H} \|u_k\|_2 \|u_k^\delta - u_k\|_2,$$

where the constant

$$\mathcal{H} = 2L_h \left(\max_{a,b} g(a,b) \sqrt{|S|} + \max_a \max_b g(a,b) \right),$$

with $g(a,b)$ the edge weight function specified in (2.3).

Proof. From triangular inequality and submultiplicativity of the operator norm, we have

$$\|\Delta_{u_k^\delta} u_k - \Delta_{u_k} u_k\|_2 \leq \|\Delta_{u_k^\delta} - \Delta_{u_k}\|_s \|u_k\|_2,$$

where $\|\cdot\|_s$ denotes the spectral norm (i.e., matrix operator norm induced by the Euclidean vector norm). We recall that, for any vector u , the graph Laplacian is given by

$$\Delta_u = D_u - W_u,$$

where the weight matrix W_u and the diagonal degree matrix D_u are same as defined in subsection 2.1. Using this result, it can be noted that

$$(3.21) \quad \|\Delta_{u_k^\delta} - \Delta_{u_k}\|_s \leq \|D_{u_k^\delta} - D_{u_k}\|_s + \|W_{u_k^\delta} - W_{u_k}\|_s.$$

Next, we individually estimate both the terms of right hand side of the above inequality, starting with the second term. For that, the entry-wise difference is

$$|w_{u_k}(a,b) - w_{u_k^\delta}(a,b)| = g(a,b) |h_{u_k}(a,b) - h_{u_k^\delta}(a,b)|,$$

where h_u is a Lipchitz continuous Gaussian kernel function for any vector u with Lipchitz constant L_h . Hence, we have that

$$\begin{aligned} |w_{u_k}(a,b) - w_{u_k^\delta}(a,b)| &= g(a,b) L_h \left(|u_k(a) - u_k(b)| - |u_k^\delta(a) - u_k^\delta(b)| \right) \\ &\leq g(a,b) L_h \left| (u_k(a) - u_k(b)) - (u_k^\delta(a) - u_k^\delta(b)) \right| \\ &\leq g(a,b) L_h \left| (u_k(a) - u_k^\delta(a)) - (u_k(b) - u_k^\delta(b)) \right| \\ &\leq g(a,b) L_h (|u_k(a) - u_k^\delta(a)| + |u_k(b) - u_k^\delta(b)|). \end{aligned}$$

Thus, we arrive at

$$\|W_{u_k^\delta} - W_{u_k}\|_F^2 \leq (\max_{a,b} g(a,b) L_h)^2 \sum_{a,b \in S} (|u_k(a) - u_k^\delta(a)| + |u_k(b) - u_k^\delta(b)|)^2,$$

where $\|\cdot\|_F$ denotes the Frobenius norm and S denotes the set associated with the edge-weight function $g(a,b)$. After solving the above estimate and using the fact that $\|\cdot\|_s \leq \|\cdot\|_F$, we get

$$(3.22) \quad \|W_{u_k^\delta} - W_{u_k}\|_s \leq \|W_{u_k^\delta} - W_{u_k}\|_F \leq 2 \max_{a,b} g(a,b) L_h \sqrt{|S|} \|u_k^\delta - u_k\|_2.$$

Similarly, we estimate the first term of (3.21) in which each diagonal entry satisfies

$$\begin{aligned} |d_{u_k}(a) - d_{u_k^\delta}(a)| &= \left| \sum_{b \in S} (w_{u_k}(a,b) - w_{u_k^\delta}(a,b)) \right| \leq \sum_{b \in S} |w_{u_k}(a,b) - w_{u_k^\delta}(a,b)| \\ &\leq \max_b g(a,b) L_h \sum_{b \in S} (|u_k(a) - u_k^\delta(a)| + |u_k(b) - u_k^\delta(b)|) \\ &\leq 2 \max_b g(a,b) L_h \|u_k - u_k^\delta\|_2. \end{aligned}$$

This yields that

$$(3.23) \quad \|D_{u_k^\delta} - D_{u_k}\|_s = \max_a |d_{u_k}(a) - d_{u_k^\delta}(a)| \leq 2 \max_a \max_b g(a, b) L_h \|u_k - u_k^\delta\|_2.$$

Plugging (3.22) and (3.23) in (3.21) to arrive at

$$\|\Delta_{u_k^\delta} - \Delta_{u_k}\|_s \leq \mathcal{H} \|u_k^\delta - u_k\|_2,$$

where \mathcal{H} is the same constant as defined in the statement. Thus, the result holds. \square

Next, we show that the Lemma 3.10, in conjunction with Assumption 3.8, establishes the stability required to link Algorithm 3.1 with Algorithm 3.2. This is formalized in the following result.

LEMMA 3.11. *Let Assumptions 3.1, 3.2 and 3.8 hold. Then for each fixed integer $k \geq 0$, there holds*

$$(3.24) \quad u_k^\delta \rightarrow u_k \quad \text{as} \quad \delta \rightarrow 0,$$

where u_k^δ and u_k are same as in Algorithm 3.1 and Algorithm 3.2.

Proof. We establish the result by induction. For the base case $k = 0$, note that $u_0^\delta = \Psi(v^\delta)$ and $u_0 = \Psi(v)$. Therefore, the claim holds trivially by Assumption 3.8. Next, let us assume that the statement holds for all $0 \leq j \leq k$. We aim to show that it also holds for $j = k + 1$, i.e., $u_{k+1}^\delta \rightarrow u_{k+1}$ as $\delta \rightarrow 0$. From (1.4), we have

$$(3.25) \quad \begin{aligned} u_{k+1}^\delta - u_{k+1} &= (u_k^\delta - u_k) - (\alpha_k^\delta A^*(Au_k^\delta - v^\delta) - \alpha_k A^*(Au_k - v)) \\ &\quad - (\beta_k^\delta \Delta_{u_k^\delta} u_k^\delta - \beta_k \Delta_{u_k} u_k). \end{aligned}$$

We begin by establishing that

$$\alpha_k^\delta A^*(Au_k^\delta - v^\delta) \rightarrow \alpha_k A^*(Au_k - v) \quad \text{as} \quad \delta \rightarrow 0.$$

To this end, we utilize that $u_k^\delta \rightarrow u_k$ and $v^\delta \rightarrow v$ as $\delta \rightarrow 0$ to establish that

$$\alpha_k^\delta = \min \left\{ \frac{\eta_0 \|Au_k^\delta - v^\delta\|^2}{\|A^*(Au_k^\delta - v^\delta)\|^2}, \eta_1 \right\} \rightarrow \min \left\{ \frac{\eta_0 \|Au_k - v\|^2}{\|A^*(Au_k - v)\|^2}, \eta_1 \right\} = \alpha_k,$$

where we have assumed $\|A^*(Au_k^\delta - v^\delta)\| \neq 0$, the case when this norm vanishes is trivial. Consequently, we obtain

$$(3.26) \quad \begin{aligned} \|\alpha_k^\delta A^*(Au_k^\delta - v^\delta) - \alpha_k A^*(Au_k - v)\| &\leq \alpha_k^\delta \|A^*(Au_k^\delta - v^\delta) - A^*(Au_k - v)\| \\ &\quad + |\alpha_k^\delta - \alpha_k| \|A^*(Au_k - v)\| \rightarrow 0 \quad \text{as} \quad \delta \rightarrow 0. \end{aligned}$$

In a similar vein, assume that $\|\Delta_{u_k^\delta} u_k^\delta\| \neq 0$. Then, by the definitions of β_k^δ and β_k , we obtain

$$\beta_k^\delta = \min \left\{ \frac{\nu_0 \|Au_k^\delta - v^\delta\|^2}{\|\Delta_{u_k^\delta} u_k^\delta\|}, \nu_1 \right\} \rightarrow \min \left\{ \frac{\nu_0 \|Au_k - v\|^2}{\|\Delta_{u_k} u_k\|}, \nu_1 \right\} = \beta_k \quad \text{as} \quad \delta \rightarrow 0.$$

This convergence follows from the induction hypothesis and Lemma 3.10, which ensures that $\|\Delta_{u_k^\delta} u_k^\delta\| \rightarrow \|\Delta_{u_k} u_k\|$ as $\delta \rightarrow 0$. Thus, we have

$$(3.27) \quad \begin{aligned} \|\beta_k^\delta \Delta_{u_k^\delta} u_k^\delta - \beta_k \Delta_{u_k} u_k\| &\leq \|\beta_k^\delta \Delta_{u_k^\delta} u_k^\delta - \beta_k^\delta \Delta_{u_k^\delta} u_k\| + \|\beta_k^\delta \Delta_{u_k^\delta} u_k - \beta_k \Delta_{u_k} u_k\| \\ &\leq \|\beta_k^\delta \Delta_{u_k^\delta} (u_k^\delta - u_k)\| + (|\beta_k^\delta - \beta_k| \|\Delta_{u_k^\delta}\| + \beta_k \|\Delta_{u_k^\delta} - \Delta_{u_k}\|) \|u_k\| \\ &\leq \|\beta_k^\delta \Delta_{u_k^\delta}\| \|u_k^\delta - u_k\| + (|\beta_k^\delta - \beta_k| \|\Delta_{u_k^\delta}\| + \beta_k \|\Delta_{u_k^\delta} - \Delta_{u_k}\|) \|u_k\|. \end{aligned}$$

Therefore, by applying Lemma 3.10 to the above expression along with the induction hypothesis, we conclude that

$$\beta_k^\delta \Delta_{u_k^\delta} u_k^\delta \rightarrow \beta_k \Delta_{u_k} u_k \quad \text{as } \delta \rightarrow 0.$$

Consequently, it follows from (3.25), (3.26), (3.27) and the induction hypothesis that $u_{k+1}^\delta \rightarrow u_{k+1}$ as $\delta \rightarrow 0$. This completes the proof. \square

3.4. Convergence for noisy data. In this subsection, our goal is to establish the regularization property of IRMGL+ Ψ method. It is worth emphasizing that, in general, convergence of the method with noisy data cannot be guaranteed, as the perturbed data v^δ may not belong to the range of the operator A , i.e., $v^\delta \notin \mathcal{R}(A)$.

THEOREM 3.12. *Under the assumptions of Lemma 3.11, if k_δ is the stopping index as defined in (1.5) for the method defined in Algorithm 3.1, then there exist a solution u^\dagger of (1.1) such that*

$$\lim_{\delta \rightarrow 0} \|u_{k_\delta}^\delta - u^\dagger\| = 0.$$

Proof. Let u^\dagger be the solution of (1.1) determined in Theorem 3.7 such that $\|u_k - u^\dagger\| \rightarrow 0$ as $\delta \rightarrow 0$, where $\{u_k\}_{k \geq 0}$ denotes the sequence of iterates determined by the Algorithm 3.2 using the exact data. We assume that there is a sequence $\{\delta_n\}$ such that $\delta_n \rightarrow 0$ as $n \rightarrow \infty$, and let v^{δ_n} be the associated noisy data sequence. The corresponding stopping index for each pair (δ_n, v^{δ_n}) , as established by (1.5), is represented by $k_n := k_{\delta_n}$. We shall examine two scenarios in order to demonstrate the desired outcome.

Case-I: Consider that for some finite integer \bar{k} , $k_n \rightarrow \bar{k}$ as $n \rightarrow \infty$. Then, for all large n , we may assume that $k_n = \bar{k}$. Consequently, using the definition of k_n , we obtain

$$(3.28) \quad \|Au_{\bar{k}}^{\delta_n} - v^{\delta_n}\| \leq \tau \delta_n.$$

Taking the limit as $n \rightarrow \infty$ in (3.28) and applying Lemma 3.11, we obtain $Au_{\bar{k}} = v$. Then, by invoking Theorem 3.7, it follows that $u_{\bar{k}} = u^\dagger$. Consequently, we conclude that $u_{k_n}^{\delta_n} \rightarrow u^\dagger$ as $n \rightarrow \infty$.

Case-II: Next, assume that there exist a sequence $\{\delta_n\}$ with $\delta_n \rightarrow 0$ such that $k_n := \hat{k}_{\delta_n} \rightarrow \infty$ as $n \rightarrow \infty$, and let v^{δ_n} be the corresponding sequence of noisy data. Let k be sufficiently large fixed integer. From Lemma 3.6, it follows that there exist an $\varepsilon > 0$ such that $\|u_k - \hat{u}\| \leq \frac{\varepsilon}{2}$. Since for fixed k , using Lemma 3.11, there is a $n = (k, \varepsilon)$ such that $\|u_k^{\delta_n} - u_k\| \leq \frac{\varepsilon}{2}$ for all $n > n(k, \varepsilon)$. Then, for sufficiently large n , such that $k_n > k$, we conclude from Lemma 3.4 that

$$\begin{aligned} \|u_{k_n}^{\delta_n} - \hat{u}\| &\leq \|u_{k_n-1}^{\delta_n} - \hat{u}\| \leq \dots \leq \|u_k^{\delta_n} - \hat{u}\| \\ &\leq \|u_k^{\delta_n} - u_k\| + \|u_k - \hat{u}\| \leq \varepsilon. \end{aligned}$$

Consequently, the outcome follows. \square

4. Numerical experiments and discussion. In this section, we present the numerical simulations for two-dimensional (2D) computed tomography (CT) and image deblurring applications. We describe the experimental setup, problem setting, and a number of numerical tests that were performed to assess the effectiveness of the IRMGL+ Ψ method. Furthermore, we provide a comparative analysis with existing methods to demonstrate the efficiency, and robustness of our approach.

4.1. X-ray Computed Tomography (CT). It is a widely used medical imaging technique that plays a crucial role in diagnosing various conditions such as internal injuries, tumors, hemorrhages, and bone fractures. A typical CT system consists of an X-ray source that rotates around the subject, emitting beams from a fixed number of angles along a circular or arc-shaped trajectory. As these X-ray beams pass through the internal structures of the body, different tissues absorb varying amounts of radiation depending on their density. The attenuated rays are then captured by a detector. See [33] for the nice details.

The set of all such measurements, acquired at multiple projection angles, is referred to as a *sinogram*. In the discrete setting, this process can be modeled by a linear system

$$A \in \mathbb{R}^{m \times n}, \quad u \in \mathcal{U} := \mathbb{R}^n, \quad v^\delta \in \mathcal{V} := \mathbb{R}^m,$$

where A denotes the discretized Radon transform (or forward operator), u represents the unknown 2D image vectorized into n pixels (or voxels), and v^δ is the vectorized sinogram obtained from noisy measurement data.

4.1.1. Experimental setup. The vectorization of the 2D image is typically performed using a lexicographic (1D) ordering of the pixels $a = (i, j)$, following either column-major or row-major convention. For an image of size $E \times F$, the total number of pixels is $n = E \cdot F$, and the image is reshaped into a vector in \mathbb{R}^n .

In [1], the Operator Discretization Library (ODL), a Python-based framework, is introduced for modeling X-ray computed tomography (CT) measurements and reconstruction. In our experiments, we utilize the function `odl.uniform_discr` to define the image domain as a uniformly discretized square grid of size $E \times F$ over the region $[-128, 128]^2 \subset \mathbb{R}^2$, represented with single-precision floating point values.

For the numerical simulation, we employ the Shepp–Logan phantom image provided by `skimage.data`. The acquisition setup is based on a parallel-beam geometry with $m_\theta = 60$ uniformly distributed projection angles over the interval $[0, 2\pi)$, constructed using the `odl.tomo.parallel.beam.geometry` routine. The forward operator $A \in \mathbb{R}^{m \times n}$, which approximates the discrete Radon transform, is implemented via `odl.tomo.RayTransform`. Here, $m = m_\theta \cdot d$, where d denotes the number of detector elements, which is automatically determined by ODL to ensure full coverage of the image domain. Specifically, for $E = F = 128$, we have $d = \lceil \sqrt{2} \cdot 128 \rceil = 363$, and hence $m = 60 \cdot 363 = 21780$, while the number of image pixels is $n = 128 \cdot 128 = 16384$ leading to an ill-conditioned linear system. For the parameter selection in the edge-weight function (2.3), we set $R = 5$ and $\sigma = 0.01$ based on empirical considerations.

In order to replicate real-world circumstances, we introduce Gaussian noise ξ into the sinogram at an intensity level of δ . In particular, we compute v^δ as

$$v^\delta = v + \delta_{rel} \|v\| \frac{\xi}{\|\xi\|},$$

where $\delta_{rel} = \|v - v^\delta\|/\|v\|$ is the relative noise level and $\delta = \delta_{rel} \|v\|$ is the noise level.

4.1.2. Reconstruction results. The primary objective of this subsection is to evaluate the reconstruction accuracy under varying noise levels using the discrepancy principle (1.5) as the stopping criterion. Similar to the investigation in [12] on various reconstruction operators Ψ for variational regularization, our iterative method also leverages a selection of initializers (excluding the NETT approach [45, 38]). Additionally, we introduce A^* (the adjoint operator) as an initializer. This choice is particularly relevant as A^* inherently satisfies Assumption 3.8, providing a fundamental,

yet non-regularizing, starting point for the reconstruction. In Fig. 6, we present the true image of Shepp-Logan Phantom and noisy sinogram.

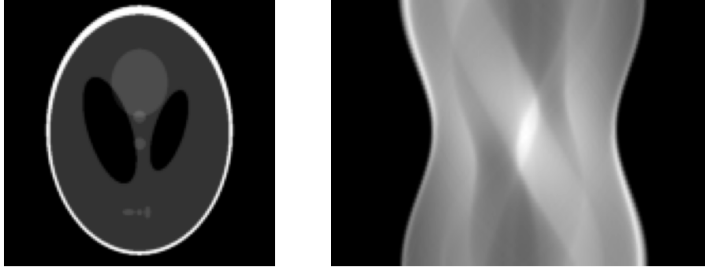


Fig. 6: Left: True phantom, Right: Noisy sinogram v^δ with $\delta = 0.05$.

Table 2: Numerical results for CT using $\text{IRMGL}+\Psi$

δ_{rel}	Metric	FBP	Adj	Tik	TV
0.1	Iterations	26	15	15	18
	Residual	1.0944e+01	9.8674e+00	9.8674e+00	1.0571e+01
0.05	Iterations	42	21	21	30
	Residual	5.4565e+00	5.1500e+00	5.1500e+00	5.3684e+00
0.01	Iterations	216	61	61	145
	Residual	1.1100e+00	1.1047e+00	1.1047e+00	1.1103e+00
0.005	Iterations	477	127	127	373
	Residual	5.4733e-01	5.4737e-01	5.4737e-01	5.4778e-01
0.001	Iterations	1000	561	561	1000
	Residual	2.4882e-01	1.0987e-01	1.0987e-01	2.3450e-01

The maximum number of iterations is set to 1000. The quantitative performance of our reconstructed images is evaluated using *Peak Signal-to-Noise Ratio (PSNR)* and the *Structural Similarity Index (SSIM)* [42]. The PSNR is given by

$$\text{PSNR}(u) := 20 \log_{10} \left(\frac{255}{\|u^\dagger - u\|_2} \right),$$

where the constant 255 corresponds to the maximum possible pixel intensity value for 8-bit grayscale images, u^\dagger denotes the ground truth image and u is the reconstructed image.

In the context of this model problem, Algorithm 3.1 is executed using noisy datasets at various noise levels. The resulting computational performance, including the required number of iterations and the achieved residual values, is summarized in Table 2.

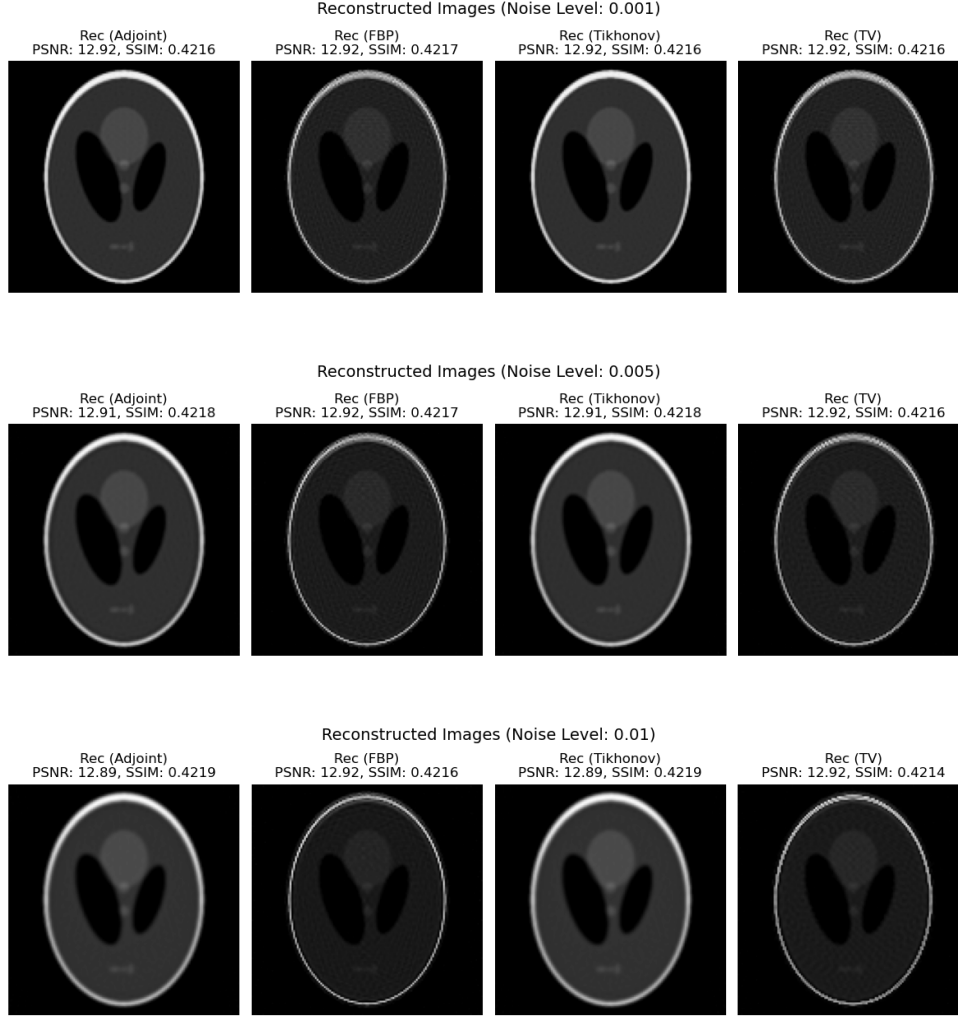


Fig. 7: Final reconstructions using $\text{IRMGL}+\Psi$ with discrepancy stopping for different noise levels, initialized with various initial reconstructors Ψ . Here ‘Rec (Ψ)’ is used to indicate the reconstruction using specific Ψ .

These findings suggest that all four initial reconstructors (Filtered Back Projection (FBP), Adjoint (Adj), Tikhonov (Tik) and Total Variation (TV)), when integrated with the $\text{IRMGL}+\Psi$ method, are capable of producing approximate solutions of comparable quality. To visually demonstrate the behavior of the discrepancy principle (1.5) as a termination rule for the proposed method, Fig. 8 displays the evolution of the residual $\|Au_{k\delta}^\delta - v^\delta\|$ with respect to the iteration count k . This analysis is conducted for data with relative noise levels of $\delta_{rel} = 0.01, 0.005$, and 0.001 , with iterations concluding upon satisfaction of the discrepancy principle or reaching a maximum of 1000 iterations.

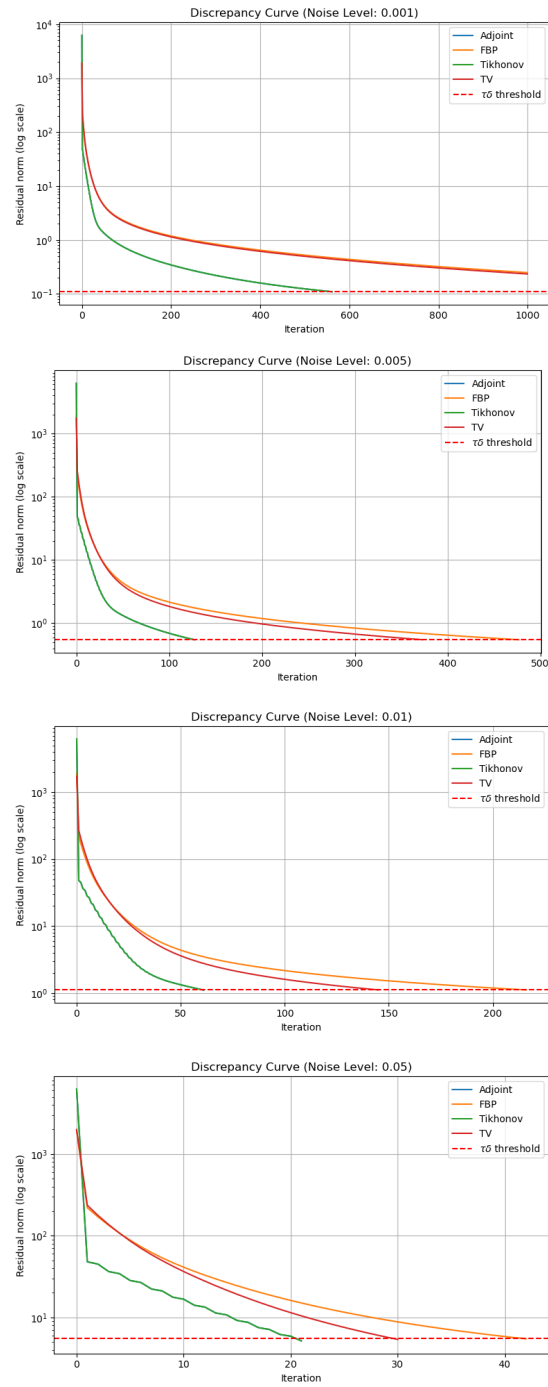


Fig. 8: Discrepancy curves for different noise levels.

As depicted in Fig. 7, we present the reconstructed images obtained at various noise levels for each of the four initial regularizers Ψ . It is noteworthy that, despite the IRMGL+ Ψ method demonstrating comparable performance and fast convergence across all initial reconstructors Ψ , initializations with $\Psi = A^*$ and $\Psi = \text{Tik}$ generally lead to superior results in the iterative process compared to others. The core issue arises from the fact that Filtered Backprojection (FBP) and Total Variation (TV) denoising are, by their nature, regularization methods. Consequently, when these are employed as initializers and then further processed by our proposed iterative regularization method, challenges such as over-regularization and a mismatch between regularization paradigms can emerge.

In the following subsection, we examine an additional example to further evaluate the performance of the proposed scheme.

4.2. Image deblurring. Consider the image deblurring problem [41], where the forward operator

$$\mathcal{A} : L^2(\Omega) \rightarrow L^2(\Omega), \quad \Omega \subset \mathbb{R}^2,$$

is defined as a spatial convolution with a Gaussian point spread function. Specially, for $u \in L^2(\Omega)$, the action \mathcal{A} is given by

$$(\mathcal{A}u)(x, y) = \int_{\Omega} G_{\rho}(x - x', y - y') \cdot u(x', y') dx' dy',$$

where the Gaussian kernel G_{ρ} is defined as

$$G_{\rho}(x, y) = \frac{1}{2\pi\rho^2} \exp\left(-\frac{x^2 + y^2}{2\rho^2}\right),$$

with $\rho > 0$ controlling the spread (or blurring strength) of the kernel.

In the experimental setup, the domain Ω is discretized into a 256×256 two-dimensional grid of pixels. The continuous forward operator \mathcal{A} is approximated by a discrete convolution operator, denoted by

$$A : \mathbb{R}^{256 \times 256} \rightarrow \mathbb{R}^{256 \times 256}.$$

Specifically, the action of A on a discrete image $u \in \mathbb{R}^{256 \times 256}$ is given by

$$(\mathcal{A}u)_{i,j} = \sum_{k,\ell} G_{\rho}(i - k, j - \ell) \cdot u_{k,\ell}, \quad i, j, k, \ell \in \{0, \dots, 255\},$$

In practice, this convolution is implemented using `scipy.ndimage.gaussian_filter` function in Python. Let $u^{\dagger} \in \mathbb{R}^{256 \times 256}$ denote the true (unknown) image. The observed data $v^{\delta} \in \mathbb{R}^{256 \times 256}$ is then modeled as

$$v^{\delta} = Au^{\dagger} + \eta, \quad \|\eta\| \leq \delta,$$

where $\eta \in \mathbb{R}^{256 \times 256}$ represents additive measurement noise, and $\delta > 0$ is the known noise level.

To reconstruct the true image u^{\dagger} from the noisy measurement v^{δ} , we apply Algorithm 3.1. In this experiment, we set $\rho = 1.5$, determining the severity of the blurring in the forward model. All other experimental parameters are consistent with those specified in Subsection 4.1.1. The effectiveness of the proposed method (1.4) under varying noise levels is illustrated in Fig. 9, Fig. 10, and Fig. 11. Additional quantitative results are provided in Table 3, which summarizes the reconstruction performance

across different noise levels, using the initial guess $u_0^\delta = A^*(v^\delta)$. The table reports the stopping index k_δ , the relative error defined by

$$\mathbf{RE} := \frac{\|u_{k_\delta}^\delta - u^\dagger\|}{\|u^\dagger\|},$$

along with the corresponding residual norms, PSNR, and SSIM, offering a comprehensive evaluation of the reconstruction quality.

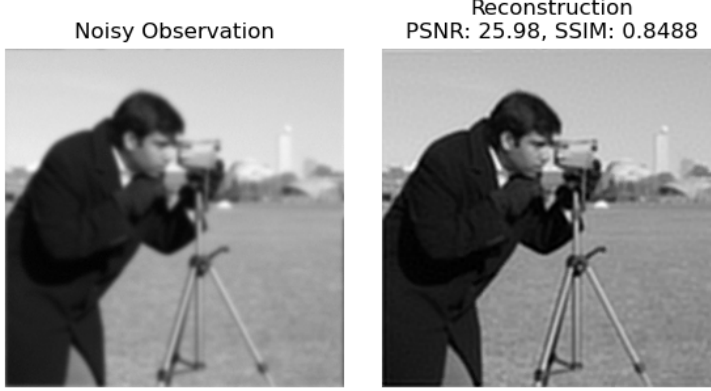


Fig. 9: Reconstructed image with $\delta = 0.005$.

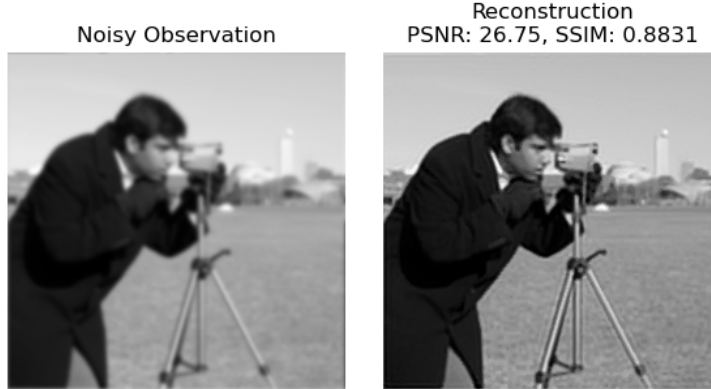
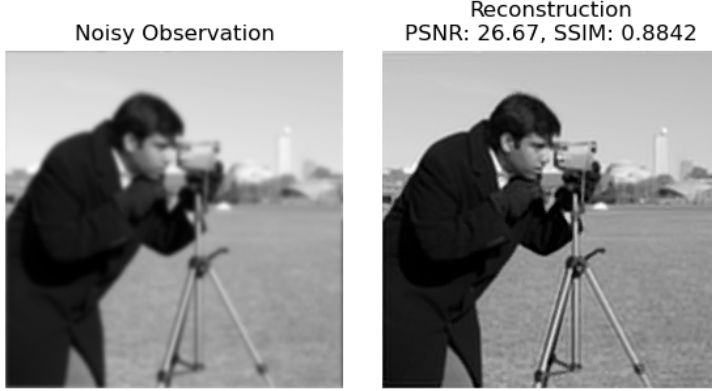


Fig. 10: Reconstructed image with $\delta = 0.001$.

4.3. Comparison Analysis. To provide a comprehensive comparison with our proposed IRMGL+ Ψ scheme, this section details the formulations of the **GraphLa+ Ψ** [12] and **it-graphLa Ψ** [11] methods. Both approaches utilize graph Laplacian regularization within a variational framework, but they differ in their handling of the updates of regularization term.

4.3.1. The GraphLa+ Ψ Method. The method, introduced in [12], is a variational regularization approach for solving inverse problems. It incorporates a graph

Fig. 11: Reconstructed image with $\delta = 0.0005$.Table 3: Numerical results of Algorithm 3.1 for image deblurring with initialization $u_0^\delta = A^*(v^\delta)$.

δ_{rel}	Iterations	Residual	RE	PSNR	SSIM
0.005	36	1.4060	0.0802	25.98	0.8488
0.003	106	0.8450	0.0821	26.46	0.8689
0.001	200	0.4167	0.0812	26.75	0.8831
0.0005	287	0.3597	0.0801	26.67	0.8842

Laplacian as a static regularization term, assuming a fixed underlying data structure. The core idea is to find the approximated solution u_β that minimizes a functional combining a data fidelity term and a Tikhonov-like regularization term weighted by a graph Laplacian. The solution u_β in this method reads

$$u_\beta \in \arg \min_{u \in \mathcal{U}} \left\{ \frac{1}{2} \|Au - v^\delta\|_2^2 + \beta \|\Delta_{\Psi_\theta^\delta} u\|_1 \right\},$$

where $\Delta_{\Psi_\theta^\delta}$ is a graph Laplacian constructed from an initial reconstruction Ψ_θ^δ . In this formulation, the graph Laplacian Δ is fixed after its initial construction based on a preliminary estimate $\Psi_\theta^\delta := \Psi_\theta(v^\delta)$ (where Ψ is a standard reconstruction operator, e.g. FBP, Tikhonov, TV).

Remark 4.1. The choice of Ψ in this method influences the initial graph structure, but the graph Laplacian itself does not evolve during the solution process.

4.3.2. The it-graphLa Ψ Method. The method, proposed in [11] specifically for acoustic impedance inversion, extends the concept of graph Laplacian regularization by introducing an iterated update of the regularization term. Unlike **GraphLa+ Ψ** , this method allows the graph Laplacian to evolve alongside the solution. The problem is typically framed as a sequence of minimization problems:

For each iteration k and regularization parameter β_k , find u_{k+1} by solving

$$\begin{cases} u_{k+1} &= \arg \min_{u \in \mathcal{U}} \left\{ \frac{1}{2} \|Au - v^\delta\|_2^2 + \beta_k \|\Delta_{u_k} u\|_1 \right\} & \text{for } k \geq 1, \\ u_0^\delta &:= \Psi(v^\delta), \end{cases}$$

where $\Psi : \mathcal{V} \rightarrow \mathcal{U}$ is the chosen initialization method.

Although the work in [11] presents numerical validation, it does not provide a rigorous theoretical justification. In contrast, our **IRMGL+ Ψ** method introduces a fully iterative and computationally efficient framework that eliminates the need for solving complex minimization problems, as required in [11, 12]. Crucially, our method addresses this theoretical shortcoming by providing rigorous proofs of convergence and stability. Moreover, the incorporation of the discrepancy principle (1.5) enhances the practical effectiveness and reliability of the algorithm.

5. Concluding remarks. This work explores the use of a graph Laplacian operator, built from an initial approximation of the solution obtained via a reconstructor Ψ , as a regularizer in iterative regularization methods for solving linearly ill-posed problems. In this method, we build a new graph Laplacian at each step, based on the previous approximation. Under certain moderate assumptions on the forward operator A and generic assumptions on Ψ , we showed that the resulting method is a stable and convergent regularization method. As a stopping rule for the approach, we examined the discrepancy principle. Irrespective of whatever reconstructor Ψ was used initially, **IRMGL+ Ψ** greatly enhanced the quality of the reconstructions in all of the numerical experiments that were presented.

There are numerous open research questions. Since this is the initial attempt to incorporate the graph Laplacian into the iterative regularization method, additional approaches such as Gauss-Newton [37], adaptive heavy ball [26], and stochastic gradient descent methods [22, 25, 24] may also be investigated. Furthermore, as a preliminary reconstruction, architectures based on deep neural networks (DNNs) can be examined.

Data Availability. The datasets and source code developed in the course of this research are available from the authors upon reasonable request.

REFERENCES

- [1] J. ADLER ET AL., *odlgroup/odl: ODL 0.7.0*, Zenodo, 2018, doi:10.5281/zenodo.1442734.
- [2] P. ARIAS, V. CASELLES, AND G. SAPIRO, *A variational framework for non-local image inpainting*, in International Workshop on Energy Minimization Methods in Computer Vision and Pattern Recognition, Springer, 2009, pp. 345–358.
- [3] S. ARRIDGE, P. MAASS, O. ÖKTEM, AND C.-B. SCHÖNLIEB, *Solving inverse problems using data-driven models*, Acta Numer., 28 (2019), pp. 1–174.
- [4] A. ASPRI, S. BANERT, O. ÖKTEM, AND O. SCHERZER, *A data-driven iteratively regularized Landweber iteration*, Numer. Funct. Anal. Optim., 41 (2020), pp. 1190–1227.
- [5] A. ASPRI, Y. KOROLEV, AND O. SCHERZER, *Data driven regularization by projection*, Inverse Problems, 36 (2020), 125009.
- [6] H. BAJPAI, G. MITTAL, AND A. K. GIRI, *Hanke-Raus heuristic rule for iteratively regularized stochastic gradient descent*, arXiv preprint arXiv:2412.02397, (2024).
- [7] H. BAJPAI, G. MITTAL, AND A. K. GIRI, *Stochastic data-driven Bouligand–Landweber method for solving non-smooth inverse problems*, J. Inverse Ill-Posed Probl., (2025).
- [8] R. BARBANO, J. ANTORÁN, J. LEUSCHNER, J. M. HERNÁNDEZ-LOBATO, B. JIN, AND Ž. KERETA, *Image reconstruction via deep image prior subspaces*, arXiv preprint arXiv:2302.10279, (2023).
- [9] D. BIANCHI, A. BUCCINI, M. DONATELLI, E. RANDAZZO, ET AL., *Graph Laplacian for Image Deblurring*, Electron. Trans. Numer. Anal., 55 (2021), pp. 169–186.

- [10] D. BIANCHI, M. DONATELLI, D. EVANGELISTA, W. LI, AND E. L. PICCOLOMINI, *Graph Laplacian and neural networks for inverse problems in imaging: Graphlanet*, in Int. Conf. on Scale Space and Variational Methods in Computer Vision, Springer, 2023, pp. 175–186.
- [11] D. BIANCHI, F. BOSSMANN, W. WANG, AND M. LIU, *Improved impedance inversion by deep learning and iterated graph Laplacian*, arXiv preprint arXiv:2404.16324, (2024).
- [12] D. BIANCHI, D. EVANGELISTA, S. ALEOTTI, M. DONATELLI, E. L. PICCOLOMINI, AND W. LI, *A data-dependent regularization method based on the graph Laplacian*, SIAM J. Sci. Comput., 47 (2025), pp. C369–C398.
- [13] M. M. BRONSTEIN, J. BRUNA, Y. LECUN, A. SZLAM, AND P. VANDERGHEYNST, *Geometric deep learning: going beyond euclidean data*, IEEE Signal Process. Mag., 34 (2017), pp. 18–42.
- [14] A. BUCCINI AND M. DONATELLI, *Graph Laplacian in $l_2 - l_q$ regularization for image reconstruction*, in 2021 Int. Conf. Comput. Sci. Appl. (ICCSA), IEEE, 2021, pp. 29–38.
- [15] L. CALATRONI, Y. VAN GENNIP, C.-B. SCHÖNLIEB, H. M. ROWLAND, AND A. FLENNER, *Graph clustering, variational image segmentation methods and Hough transform scale detection for object measurement in images*, J. Math. Imaging Vis., 57 (2017), pp. 269–291.
- [16] H. W. ENGL, M. HANKE, AND A. NEUBAUER, *Regularization of Inverse Problems*, vol. 375, Springer, 1996.
- [17] G. GILBOA AND S. OSHER, *Nonlocal linear image regularization and supervised segmentation*, Multiscale Model. Simul., 6 (2007), pp. 595–630.
- [18] G. GILBOA AND S. OSHER, *Nonlocal operators with applications to image processing*, Multiscale Model. Simul., 7 (2009), pp. 1005–1028.
- [19] M. HANKE, A. NEUBAUER, AND O. SCHERZER, *A convergence analysis of the Landweber iteration for nonlinear ill-posed problems*, Numer. Math., 72 (1995), pp. 21–37.
- [20] P. C. HANSEN, J. G. NAGY, AND D. P. O’LEARY, *Deblurring Images: Matrices, Spectra, and Filtering*, SIAM, 2006.
- [21] A. K. JAIN, *Fundamentals of Digital Image Processing*, Prentice-Hall, 1989.
- [22] T. JAHN AND B. JIN, *On the discrepancy principle for stochastic gradient descent*, Inverse Probl., 36 (2020), 095009.
- [23] T. JAHN AND B. JIN, *Early stopping of untrained convolutional neural networks*, SIAM J. Imaging Sci., 17 (2024), pp. 2331–2361.
- [24] B. JIN, Z. ZHOU, AND J. ZOU, *On the convergence of stochastic gradient descent for nonlinear ill-posed problems*, SIAM J. Optim., 30 (2020), pp. 1421–1450.
- [25] B. JIN AND Ž. KERETA, *On the convergence of stochastic gradient descent for linear inverse problems in Banach spaces*, SIAM J. Imaging Sci., 16 (2023), pp. 671–705.
- [26] Q. JIN AND Q. HUANG, *An adaptive heavy ball method for ill-posed inverse problems*, SIAM J. Imaging Sci., 17 (2024), pp. 2212–2241.
- [27] B. KALTENBACHER, A. NEUBAUER, AND O. SCHERZER, *Iterative Regularization Methods for Nonlinear Ill-posed Problems*, Walter de Gruyter, 2008.
- [28] A. C. KAK AND M. SLANEY, *Principles of Computerized Tomographic Imaging*, SIAM, 2001.
- [29] M. KELLER, D. LENZ, AND R. K. WOJCIECHOWSKI, *Graphs and Discrete Dirichlet Spaces*, vol. 358, Springer, 2021.
- [30] Y. LOU, X. ZHANG, S. OSHER, AND A. BERTOZZI, *Image recovery via nonlocal operators*, J. Sci. Comput., 42 (2010), pp. 185–197.
- [31] G. MITTAL, H. BAJPAI, AND A. K. GIRI, *Convergence analysis of iteratively regularized Landweber iteration with uniformly convex constraints in Banach spaces*, J. Complexity, 86 (2025), 101897.
- [32] V. MOROZOV, *On the solution of functional equations by the method of regularization*, Dokl. Akad. Nauk SSSR, 167 (1966), pp. 510.
- [33] F. NATTERER, *The Mathematics of Computerized Tomography*, SIAM, 2001.
- [34] M. K. NG, R. H. CHAN, AND W.-C. TANG, *A fast algorithm for deblurring models with Neumann boundary conditions*, SIAM J. Sci. Comput., 21 (1999), pp. 851–866.
- [35] G. PEYRÉ, S. BOUGLEUX, AND L. COHEN, *Non-local regularization of inverse problems*, in Computer Vision–ECCV 2008, Springer, 2008, pp. 57–68.
- [36] G. PEYRÉ, S. BOUGLEUX, AND L. D. COHEN, *Non-local regularization of inverse problems*, Inverse Probl. Imaging, 5 (2011), pp. 511–530.
- [37] Q. JIN, *On the iteratively regularized Gauss-Newton method for solving nonlinear ill-posed problems*, Math. Comp., 69 (2000), pp. 1603–1623.
- [38] O. RONNEBERGER, P. FISCHER, AND T. BROX, *U-net: Convolutional networks for biomedical image segmentation*, in MICCAI 2015, Springer, 2015, pp. 234–241.
- [39] O. SCHERZER, *A modified Landweber iteration for solving parameter estimation problems*, Appl. Math. Optim., 38 (1998), pp. 45–68.
- [40] O. SCHERZER, M. GRASMAIR, H. GROSSAUER, M. HALTMEIER, AND F. LENZEN, *Variational*

- Methods in Imaging*, vol. 167, Springer, 2009.
- [41] C. R. VOGEL, *Computational Methods for Inverse Problems*, SIAM, 2002.
 - [42] Z. WANG, A. C. BOVIK, H. R. SHEIKH, AND E. P. SIMONCELLI, *Image quality assessment: from error visibility to structural similarity*, IEEE Trans. Image Process., 13 (2004), pp. 600–612.
 - [43] H. WANG, T. LI, Z. ZHUANG, T. CHEN, H. LIANG, AND J. SUN, *Early stopping for deep image prior*, Trans. Mach. Learn. Res., (2023).
 - [44] X. ZHANG, M. BURGER, X. BRESSON, AND S. OSHER, *Bregmanized nonlocal regularization for deconvolution and sparse reconstruction*, SIAM J. Imaging Sci., 3 (2010), pp. 253–276.
 - [45] D. EVANGELISTA, E. MOROTTI, AND E. L. PICCOLOMINI, *RISING: A new framework for model-based few-view CT image reconstruction with deep learning*, Comput. Med. Imaging Graph., 103 (2023), 102156.